J. Fluid Mech. (1996), *vol.* 327, *pp.* 393–409
Copyright © 1996 Cambridge University Press

Melting of a sphere in hot fluid

By PAUL McLEOD[1], DAVID S. RILEY[2] AND R. STEPHEN. J. SPARKS[1]

[1] Department of Geology, University of Bristol, Wills Memorial Building, Queen's Road, Bristol, BS8 1RJ, UK

[2] Department of Theoretical Mechanics, University of Nottingham, University Park, Nottingham, NG7 2RD, UK

(Received 23 January 1995 and in revised form 3 May 1996)

Solid bodies immersed in hot fluids may melt. The molten material produced can then mix with, and be assimilated into, the fluid influencing its compositional and thermal states. Compositional convection of melt and thermal convection of cooled fluid around the solid determine the heat flux from the fluid to the solid's surface. This, together with the thermal properties of the solid, controls the rate of melting. Experiments on melting wax spheres into water are described; these have shown how variations in the nature of melt flow round the sphere cause differing melting rates and hence the development of a distinctive melting morphology. Melting rates are calculated by a simple theoretical analysis which estimates melt layer thickness and the heat flux from the fluid. Melting rate predictions agree well with the experimental data. A geological application occurs when magma incorporates blocks of its surrounding wall rock. Relatively rapid melting rates are estimated, typically in the order of a half metre per day. Such fast rates indicate that this method of contamination may be an important influence on magmatic evolution in continental environments.

1. Introduction

When solid objects are incorporated into a hot fluid, with a temperature higher than the melting temperature of the solid, they will melt, producing molten material that can mix with and contaminate the surrounding fluid. The rate and extent of melting will influence both the fluid's thermal and compositional evolution.

The melting of walls, floor and roof of a container which encloses hot fluid has been studied previously. Campbell & Turner (1987) and Huppert & Sparks (1988*a*, *b*) described roof melting, and Huppert & Sparks (1988*c*) considered melting of the floor. These studies noted that the density contrast between fluid and melt will result either in the melt sinking into and mixing with the fluid, producing a hybrid, homogenous liquid, or the melt pooling at the roof or floor in a layer that thickens as melting proceeds. In this latter case little mixing occur and the chamber margins become more insulated from the hot fluid as the layer grows. A theoretical analysis was developed by Huppert & Sparks (1988*a*, *b*) to describe melting of the container roof. Kerr (1994*a*) considered melting of the chamber margins further and presented an analysis appropriate to melting on the floor and sloping margins (i.e. walls) of the container. The single-boundary-layer model of melting the sloping roof of a chamber was extended to melting spheres and cylinders (Kerr 1994*a*).

This present work concerns the melting of solid spheres immersed in a hot fluid. The study is mainly confined to the case of stationary spheres submerged in a fluid that is

Specific heat of melt and solid, c	2500	J kg^{-1} °C^{-1}
Thermal conductivity of melt, k	0.202	J m^{-1} s^{-1} °C^{-1}
Enthalpy of melting, L	146000	J kg^{-1}
Melting temperature, T_f	20	°C
Melt density, ρ	1123	kg m^{-3}

TABLE 1. Properties of PEG 600

free to convect and is therefore relevant to situations where the solid is neutrally buoyant. When the melt and fluid are of different compositions, there will be a density contrast resulting in compositional convection of the melt. This may be expected to have a significant influence on the melting process, in contrast to the cases of ice melting into water (e.g. Schenk & Schenkels 1968), or solid benzene into liquid benzene (Kranse & Schenk 1965).

A geological example of this process is when the margins of a magma chamber fracture and blocks of the surrounding rock (xenoliths) are incorporated into the magma. Melting and assimilation of these will alter the magma composition and lower its temperature, thus affecting magmatic dynamics and the nature of the resultant rock.

Analogue experiments have been conducted which have facilitated observations of the melting processes and allowed quantitative measurements to be made. The experimental technique used is briefly outlined in §2, followed by a qualitative account of the phenomena that occur when spheres melt, and then the melting data are presented. Simple theoretical models are developed (§4) which predict the melting rate of a sphere immersed in a hot fluid. Comparison of theoretically predicted and experimentally measured rates (§5) shows that there is good agreement. The theoretical model is applied to geological systems in §6.

2. Experimental technique

The experiments consisted of melting wax spheres of about 5 cm diameter in water; the melt produced was always denser than the surrounding water. They were conducted in a large Perspex tank, of dimensions 50 cm by 50 cm by 1 m height. This volume, water-filled, was sufficient from there to be no variations in the far-field conditions throughout the experiments. The water was heated to a uniform temperature, which ranged between 20 and 60 °C, and then left to stand for ~ 10 minutes to allow motions to subside before commencing the experiments. One additional experiment was conducted using aqueous $NaNO_3$ solution (density 1175 kg m^{-3}) instead of pure water; this was done to compare the case where the melt was less dense than the surrounding fluid.

The wax was polyethylene glycol 600 (PEG 600), which is water soluble. Its relevant properties are listed in table 1 and the viscosity variation with temperature is shown in figure 1. Solid spheres were made by pouring molten PEG 600 into tennis ball moulds and leaving them to freeze. For all experiments the initial temperature of the solid PEG 600 was -17 °C. The spheres were attached to a supporting frame by threads, which was then rapidly immersed so that the spheres were suspended underwater in a stationary mid-tank position (figure 2). The experiments were recorded by video so that measurements of their dimensions as spheres melted and dissolved could be taken from the images on the TV screen. The accuracy of these measurements is $\sim \pm 0.5$ mm.

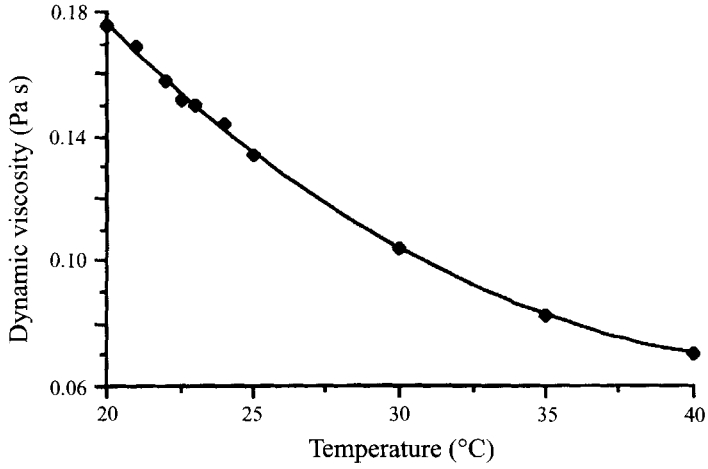

FIGURE 1. Dynamic viscosity of PEG 600 melt as a function of temperature (personal communication from Mark Stasiuk).

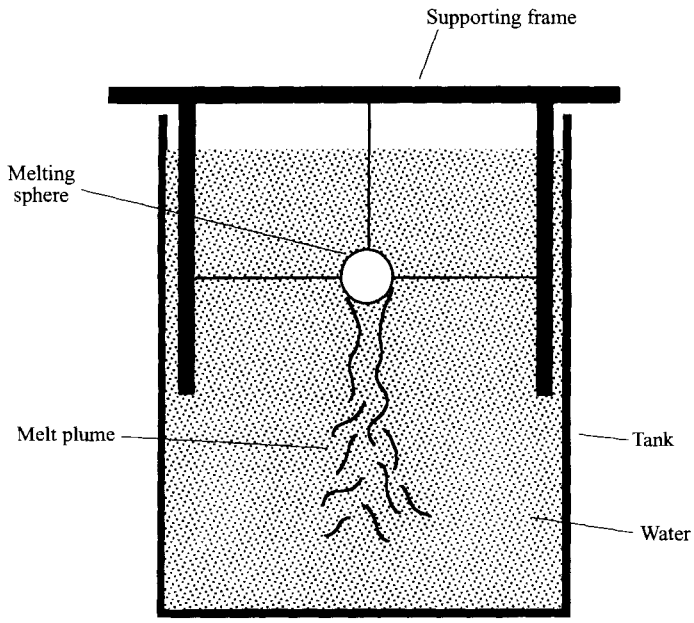

FIGURE 2. Experimental apparatus.

3. Experimental observations

3.1. *Qualitative description of melting phenomena*

The water and $NaNO_3$ solution will be referred to as fluid and molten PEG 600 as the melt. Most of the experiments were with water and so these will dominate the descriptions here; where the $NaNO_3$ solution experiment is described it will be noted explicitly.

Upon immersion into hot fluid, the solid PEG sphere began to melt, forming a thin layer of melt over its surface. The melt was denser than water and sank. On the sphere's upper surface the layer flowed downwards as a thin sheet. The thickness of this sheet was assessed by eye to be roughly 0.5 mm when the fluid was hottest (60 °C), and

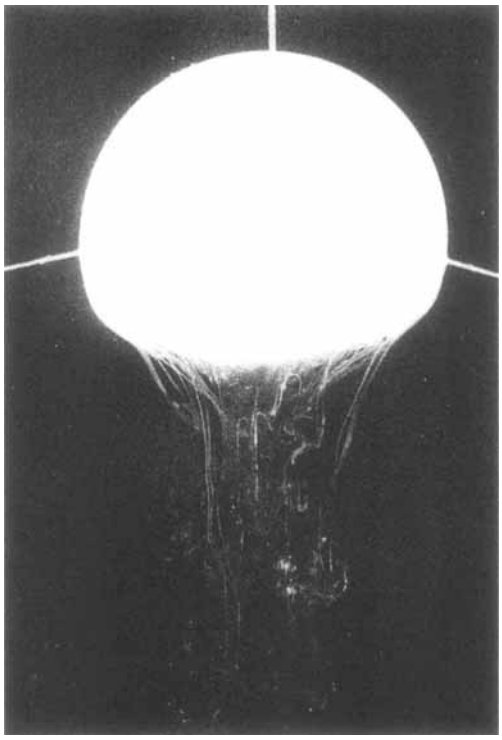

FIGURE 3. Photograph of a PEG sphere during a melting experiment. Melt fingers detach from the underside and merge into a turbulent plume; compositional convection on the upper hemisphere is not discernible due to the small thickness of the melt sheet. Upon melting the sphere develops an asymmetric morphology

slightly thinner when the fluid was cooler. Melt detached from the sphere's underside to form numerous elongated melt fingers, which immediately sank into the water. The rate of sinking was estimated to be faster than 1 cm s^{-1}, possibly as much as 3 or 4 cm s^{-1}. There were typically $\sim$ 40 fingers (up to 1 mm wide), which intermingled and merged into a plume. The fingers were initially laminar but then after a few centimetres accelerated, became unstable, and merged together to form a turbulent plume. Figure 3 is a photograph of a typical experiment and figure 4 is a diagram illustrating the nature of the flow of melt around the sphere. A gentle spiralling motion was observed in the plume, probably initiated by vestigial fluid movements in the tank.

When methylene blue crystals were dropped onto the sphere they left dye trails in the fluid as they fell. These were bent round confirming the existence of a convective thermal boundary layer adjacent to the cold sphere. The laminar flow of cooled fluid sank around the sphere, detached from under the lower half of the sphere and sank away as a plume.

The initial detachment of the melt layer was $\sim$ 1 cm below the sphere's equator. This delayed separation was caused by the radially inwards component of motion of the thermal boundary layer which swept the melt layer onto the underside of the sphere.

The sphere developed a distinctive morphology. Where melt flowed as a uniform sheet on the upper hemisphere and on the top section of the lower hemisphere, the surface remained smooth. The sphere's upper half remained essentially hemispherical, although it did eventually acquire a slightly flattened shape as the melting rate at the upper pole of the sphere was slightly faster than at the equator. At the level of melt

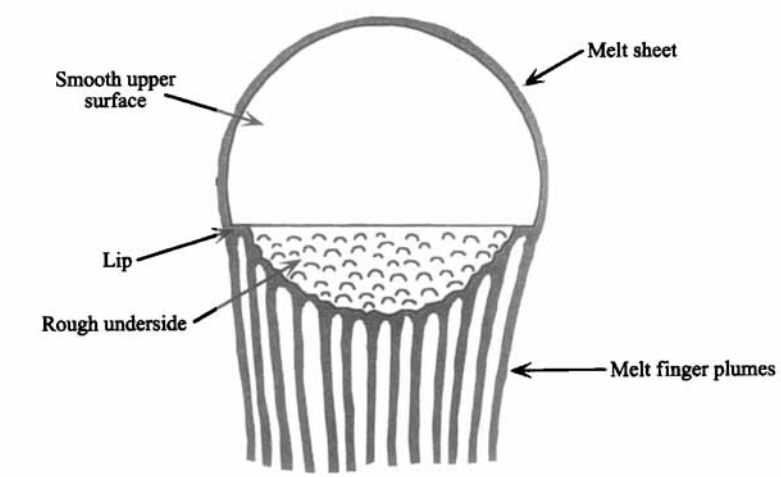

FIGURE 4. Schematic representation of a melting sphere's morphology and the compositional convective flow of melt. Thicknesses of melt layers has been exaggerated.

sheet detachment a lip formed ($\sim$ 2 mm wide) and below this the surface became rough and pitted (figure 4). The melting rate in the region of finger convection on the lower hemisphere was faster than on the upper hemisphere, so that the shape of the sphere became vertically asymmetric (see figures 3 and 4).

The upper hemisphere morphology, and the flow of melt and cooled fluid was symmetrical around the vertical axis of the sphere. Melting on the underside of the lip caused it to gradually erode back up the sphere throughout the experiments; when the spheres fragmented at the end of experiments the lips were generally close to the equator. In all cases the sphere fragmented before completely melting due to contraction fractures which formed upon freezing.

The experiment conducted using $NaNO_3$ solution produced quite similar phenomena to the experiments done with water, except that in this case the melt was positively buoyant. Apart from being inverted, the melt flow regimes, and the sphere's acquired morphology were similar to that described above. There were two small differences in the compositional convection: there is no delayed detachment of the melt layer (i.e. it detached from the sphere's equator), and the plume tended to become turbulent sooner; this second point could be due to the opposing flow of the fluid's downwards thermal convection. The different relative motion of melt to the fluid thermal-boundary-layer flow induced no other effect.

Assimilation of melt into the fluid to form a mixture of hybrid composition occurs in two stages: first melt is produced, and then it is dissolved into the fluid. This second step takes place by diffusion across the melt–fluid interface. Melt dissolution occurred to a small extent as melt flowed around the sphere and is detectable from the quantitative data. However, most of the melt produced dissolved when it fell away in the plume; here mechanical mixing rapidly enlarged the melt–fluid interface area and accelerated dissolution. The turbulent flow mixed melt efficiently with the fluid. The melt is dissolved as quickly as it is produced, so the rate-controlling step of the sphere's assimilation is melting and not dissolution of melt. Because the majority of melt dissolution occurred in the plume away from the sphere, heat released by dissolution did not influence the melting process.

It seems reasonable to assume that the flow in the outer free convective thermal boundary layer determines the heat flux from the fluid. The heat flux to the sphere's

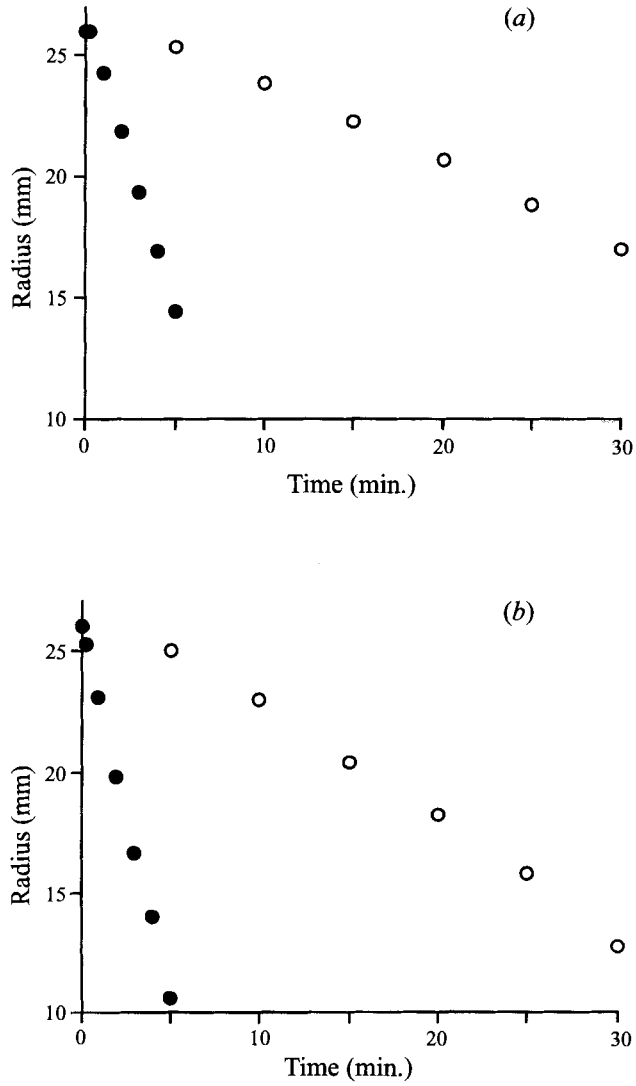

FIGURE 5. Typical experimental measurements of the change in sphere radius with time on (*a*) the sheet flow hemisphere $\theta = \frac{1}{4}\pi$, $T_w = 60$ °C (●) and 25 °C (○); and (*b*) the detaching plume hemisphere $\theta = \pi$, $T_w = 60$ °C (●); $\theta = \frac{3}{4}\pi$, $T_w = 25$ °C (○).

surface is related to the thermal gradient across the melt layer, which is influenced by the layer thickness. For example, a thin layer will have a steeper thermal gradient and so a higher heat flux which produces a faster rate of melting. The smooth hemispherical surface of the upper solid is a result of the melt forming a sheet of roughly constant thickness, and a consequential roughly uniform melting rate. Similarly, the rough morphology of the lower hemisphere is a consequence of the unstable compositional convection generating local fluctuations in melt layer thickness and melting rate, which result in morphological instability, i.e. where melt is detaching as a plume the layer is far thicker and so melting slower, while between these points the layer is thinner, and the resultant faster melting causes a pit to develop. Similar pitting structures have been observed on planar melting interfaces (Campbell 1986; Fang & Hellawell 1988; Kerr 1994*a*).

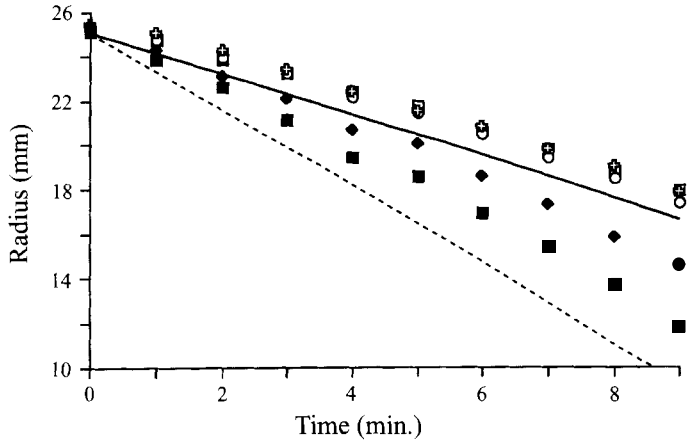

FIGURE 6. Changes in sphere radius with time for the case where $NaNO_3$ solution is the fluid (at 40 °C). Experimental data for the detaching plume hemisphere are shown by filled symbols (■, $\theta = 0$; ◆, $\theta = \frac{1}{4}\pi$), and data for the sheet flow hemisphere by open symbols (✚, $\theta = \frac{1}{2}\pi$; ○, $\theta = \frac{3}{4}\pi$; and □, $\theta = \pi$). Theoretical estimates are shown by dotted (detaching plume hemisphere) and the solid (sheet flow hemisphere) lines.

Clearly, the melting sphere can be divided into two hemispheres on the basis of the melt flow regimes and resulting morphology. The hemisphere where melt flows as a sheet, which was the upper one in the experiments where water was the fluid (negatively buoyant melt) and the lower hemisphere in the experiment where $NaNO_3$ solution was the fluid (positively buoyant melt), will be termed the sheet flow hemisphere. The other half of the sphere where melt detached as finger plumes, will be termed the detaching plume hemisphere.

3.2. *Quantitative results*

Measurements of the change in sphere radius with time during two experiments are shown in figure 5. The experiments were both with water as the fluid, at ambient temperatures (T_w) of 25 and 60 °C. Measurements taken on the sheet flow hemisphere are presented in figure 5(*a*), and those for the detaching plume hemisphere in figure 5(*b*). The data are of radii at various orientations, θ is the colatitude angle measured from the north pole of the sphere so that $\theta = \frac{1}{2}\pi$ is the spheres' equator, etc. The data from the $NaNO_3$ solution experiment are shown in figure 6. The theoretical predictions of melting rates are also presented; the derivation of these will be described later.

The data show that there is an initial, brief period when the melting rate increases slightly, after this the rate stabilizes and remains essentially constant.

The relationship between the melting rates measured during the water experiments and the temperature difference between the ambient fluid (T_w) and the solid's melting point (T_f) are shown in figure 7. Theoretical predictions of melting rates, as discussed below, are also included. In all experiments rates are very low (0.005 to 0.06 mm s^{-1}). Melting on the detaching plume hemisphere is slightly faster than on the sheet flow hemisphere. Comparison of melting rates on the sheet flow hemisphere for different radii orientations shows that there is a slight decrease from $\theta = 0$ to $\frac{1}{2}\pi$; the maximum variation is $\sim 20\,\%$ at the highest temperature contrast.

PEG 600 is water soluble and this is evident in figure 7 where there is a small 'melting' rate when the fluid temperature is at the solid's melting point ($T_w - T_f = 0$ °C). This is in fact a dissolution rate (Kerr 1994*b*); it is, however, small compared to the rate of melting and so is of little importance.

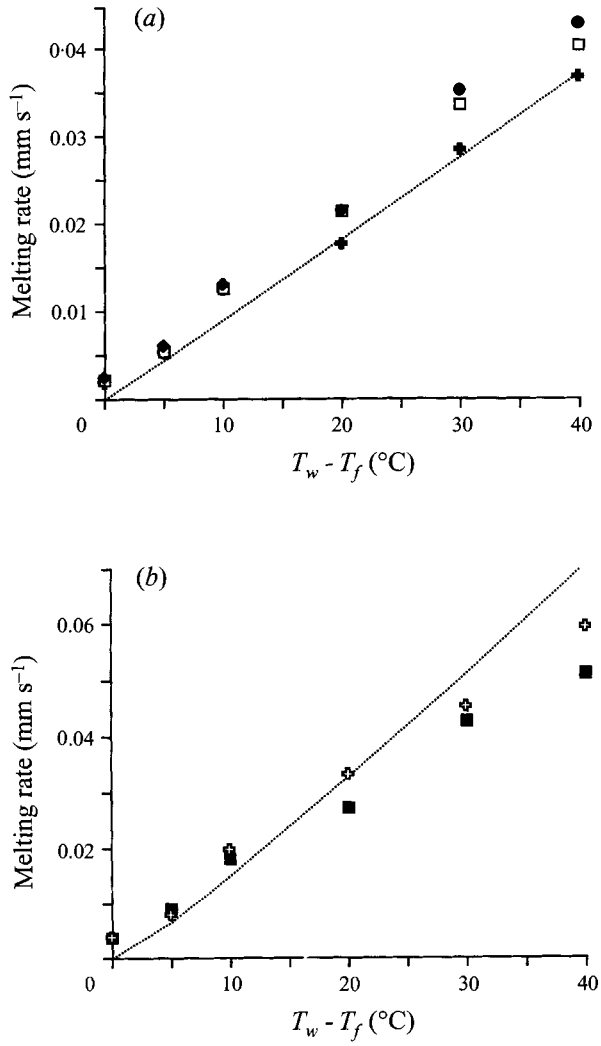

FIGURE 7. Melting rates at various orientations on (*a*) the sheet flow hemisphere, and (*b*) the detaching plume hemisphere. Experimental measurements are shown by the points and the theoretical estimates by the dotted lines. (*a*) ◆, $\theta = 0$; □, $\theta = \frac{1}{4}\pi$; ✚, $\theta = \frac{1}{2}\pi$. (*b*) ✚, $\theta = \frac{3}{4}\pi$; ■, $\theta = \pi$.

4. Theory

The experimental results suggest that, after initial transients have died away, there is a substantial period of slow, steady evolution. It is this period of evolution of the sheet flow that we aim to describe through a simple mathematical model. The key assumptions that we make are that:

(i) the melting front is spherically symmetric;

(ii) the melt flow is independent of longitudinal angle and there is no swirl;

(iii) the melt thickness is much less than the solid hemisphere's radius (lubrication approximation holds);

(iv) the melting time scale is much longer than the typical flow time scales (quasi-static assumption);

(v) the effect of change of volume upon melting is neglected.

On balancing viscous and gravitational forces there results a characteristic velocity

scale $V = g'\delta_0^2/\nu$, where δ_0 is the characteristic melt thickness. Here ν is the kinematic viscosity of the melt and g' denotes reduced gravity, $g\Delta\rho/\rho$, where $\Delta\rho$ is the contrast between the density of the melt ρ and that of the surrounding water. The melt thickness δ_0 is determined by the thermal processes. On balancing convection and conduction in the melt (since the Péclet number is large), $\delta_0^2 = \kappa a/V$ where a is the initial radius of the solid sphere and κ is the thermal diffusivity of the melt. Hence

$$\delta_0 = \left(\frac{\nu\kappa a}{g'}\right)^{1/4} \quad \text{and} \quad V = \left(\frac{g'\kappa a}{\nu}\right)^{1/2}; \tag{1}$$

$\nu = 1.6\times10^{-4}\ \mathrm{m^2\,s^{-1}}$, $\kappa = 7.2\times10^{-8}\ \mathrm{m^2\,s^{-1}}$, $a = 2.6\times10^{-2}$ m, and $g' = 1.07\ \mathrm{m\,s^{-2}}$ and therefore

$$V \sim 3.5\times10^{-3}\ \mathrm{m\,s^{-1}}, \quad \delta_0 \sim 7.2\times10^{-4}\ \mathrm{m}.$$

The longest time scale in the problem is that associated with the latent-heat condition at the solid/melt interface. Thus the characteristic time scale τ is given by

$$\tau = \frac{a\delta_0 L}{\kappa c(T_w - T_f)}, \tag{2}$$

where L is the latent heat per unit mass, c the specific heat and T_f the fusion temperature of the solid; T_w denotes the ambient water temperature. Hence $\tau \sim 3\times10^3$ s.

The above scales are consistent with the experiment results: recall that the thickness of the melt sheet was estimated to be ~ 0.5 mm, whilst, in the experiment with the ambient temperature of the water set at 25 °C, 9 mm of the solid melted in 1800 s (figure 5*a*), which is a rate consistent with the characteristic rate of 26 mm of solid melting in 3000 s.

In the mathematical model we work relative to a spherical polar coordinate system (r, θ, λ) where λ is the longitudinal angle and θ measures colatitude, with the north pole of the sphere at $\theta = 0$. In view of the axisymmetric assumption it is convenient to measure radial position relative to the solid/melt interface $r = S(t)$ by using

$$y = \frac{r - S(t)}{\delta(\theta, t)}, \tag{3}$$

where δ is the local film thickness. Applying standard lubrication theory yields

$$\frac{\partial v_r}{\partial y} + \frac{\delta}{S\sin\theta}\frac{\partial}{\partial\theta}(v_\theta \sin\theta) - \frac{1}{S}\frac{\partial\delta}{\partial\theta}\frac{\partial v_\theta}{\partial y} = 0, \tag{4}$$

$$\frac{-1}{\rho S}\frac{\mathrm{d}P}{\mathrm{d}\theta} + \frac{\nu}{\delta^2}\frac{\partial^2 v_\theta}{\partial y^2} + g'\sin\theta = 0, \tag{5}$$

$$\frac{\kappa}{\delta}\frac{\partial^2 T}{\partial y^2} = \left(v_r + m - y\frac{\partial\delta}{\partial t} - \frac{y}{S}\frac{\partial\delta}{\partial\theta}v_\theta\right)\frac{\partial T}{\partial y} + \frac{\delta}{S}v_\theta\frac{\partial T}{\partial\theta}, \tag{6}$$

where $(v_r, v_\theta, 0)$ and T represent the velocity and temperature, respectively, in the melt, P denotes dynamic pressure and $m = -\mathrm{d}S/\mathrm{d}t$ is the quasi-static rate of melting of the sphere. These equations are valid in the limit $a/V\tau \to 0$, $\delta/a \to 0$ and $R \to 0$, where R denotes the reduced Reynolds number $V\delta_0^2/a\nu$.

In (5), the pressure field is determined by that in the surrounding flow of cooled water. Since this flow is natural convection, the dynamic pressure in the streamwise direction may be taken to be negligible small. Thus

$$\frac{\mathrm{d}P}{\mathrm{d}\theta} = 0, \tag{7}$$

allowing simple integration of (5) to give

$$v_\theta = \frac{\delta^2 g'}{\nu}(y - \tfrac{1}{2}y^2)\sin\theta, \tag{8}$$

satisfying no-slip at the solid/melt interface and the assumption of zero stress at the melt/water interface (a condition suggested by the consistency of the results from the coflowing and countercurrent cases, despite the viscosities of the water and melt being of the same order). Having found the longitudinal flow, the radial flow field follows from the equation of continuity (4):

$$v_r = \frac{g'}{\nu S \sin\theta}\left\{\delta(\tfrac{1}{6}y^3 - \tfrac{1}{2}y^2)\frac{\partial}{\partial\theta}(\delta^2\sin^2\theta) + \delta^2\sin^2\theta\frac{\partial\delta}{\partial\theta}(\tfrac{1}{2}y^2 - \tfrac{1}{3}y^3)\right\}, \tag{9}$$

satisfying $v_r = 0$ at $y = 0$. Now at the edge of melt layer, $y = 1$, $v_r = -m$ which gives a differential equation for δ. Solving this equation subject to δ being well behaved as $\theta \to 0$ yields

$$\delta^3 = \frac{2m\nu S}{g'}\frac{(2+z)}{(1+z)^2}, \tag{10}$$

where $z = \cos\theta$; m is assumed constant over the hemisphere. Substituting (10) back into (9), yields

$$v_r = \frac{\tfrac{1}{3}my^2(-5z^2 + 2z^2y - 10z + 4zy - 3)}{(1+z)^2}. \tag{11}$$

From (10), the average film thickness over the upper hemisphere is found to be

$$\bar{\delta} = 1.4\left(\frac{m\nu S}{g'}\right)^{1/3}. \tag{12}$$

Having found the flow field and film thickness in terms of the unknown melting rate m, we can now turn to (6) and solve from the thermal field. In terms of the independent variables y and z ($z = \cos\theta$), the equation for T is

$$\frac{\kappa}{\delta}\frac{\partial^2 T}{\partial y^2} = \left(v_r + m + \frac{my\delta}{3S} + \frac{y}{S}(1-z^2)^{1/2}\frac{\partial\delta}{\partial z}v_\theta\right)\frac{\partial T}{\partial y} - \frac{\delta}{S}(1-z^2)^{1/2}v_\theta\frac{\partial T}{\partial z}, \tag{13}$$

with v_r, v_θ and δ given by (11), (12) with $\sin\theta = (1-z^2)^{1/2}$ and (10), respectively. The equations must be solved subject to: $T = T_f$, the fusion temperature of the PEG, at $y = 0$; $T = T_{mw}(\theta, t)$, the melt/water interface temperature, at $y = 1$; and $\partial T/\partial z$ bounded as $z \to 1-$.

The interface temperature distribution T_{mw} should be determined by coupling the melt problem with a study of the free convection of the surrounding water. This is clearly a very substantial problem and the effort required is incommensurate with the accuracy of our experimental data. We therefore adopt a pragmatic approach: we solve for the temperature in the melt by applying a Kármán–Pohlhausen method (or, as it is generally known in the heat transfer literature, Goodman's heat-balance technique), We then average the resulting thermal field over the upper hemisphere to obtain a representative interfacial temperature $T_i = \bar{T}_{mw}$; this in turn is fed in to Nusselt number correlations for steady free convection around isothermal spheres and related to the thermal flux through the melt.

In fact, for simplicity of presentation we take a more direct approach which is equivalent to the above when a temperature profile that is linear in y is used in the

Kármán–Pohlhausen method. Assuming sufficient regularity of the Kármán–Pohlhausen solution, the process of averaging eventually yields a thermal field of the form

$$T = T_f + y(T_i - T_f), \tag{14}$$

where T_i is an unknown interfacial temperature which is slowly varying in time. Thus the thermal flux in the inward radial direction, F_m say, is uniform across the melt layer, and

$$F_m = k\frac{T_i - T_f}{\bar{\delta}}, \tag{15}$$

where k is the thermal conductivity of the metal and $\bar{\delta}$ is the average film thickness given by (12).

The Nusselt number correlation that we choose to use is one derived by Jafarpur & Yovanovich (1992) for steady free convection of large-Prandtl-number fluids about isothermal spheres. Three remarks are pertinent here:

(i) The Prandtl number for water, which is about 7, is large enough for their asymptotic formula to be reasonably accurate.

(ii) The correlation formula is derived from a linearized energy equation involving a characteristic velocity. This characteristic velocity does not take direct account of the nature of the sphere's surface (i.e. whether it is non-slip or stress-free).

(iii) It is reasonable to use a correlation for steady convection since quantities are slowly varying in the present problem.

On applying continuity of heat flux at the melt/water interface we obtain

$$F_m = \frac{k_w(T_w - T_i)}{2S}(2 + 0.6\,\mathrm{Ra}^{1/4}), \tag{16}$$

where we have taken the sphere to have radius S. The subscript w refers to values for water,

$$\mathrm{Ra} = \frac{g\beta_w(T_w - T_i)(2S)^3}{\nu_w \kappa_w}, \tag{17}$$

β_w is the coefficient of cubical expansion and the rest of the nomenclature is as before. Equating (15) and (16) determines T_i for given film thickness $\bar{\delta}$ and radius S. Now $\bar{\delta}$ is given by (12) in terms of m (since S is determined one m is known). Thus we need another relation to fix m.

This relation follows by considering the latent heat condition at the solid/melt interface $r = S$:

$$-k\frac{\partial T}{\partial r} + k\frac{\partial T_s}{\partial r} = \rho L\frac{\mathrm{d}S}{\mathrm{d}t} = -\rho L m, \tag{18}$$

where constancy of thermophysical properties on change of state has been assumed; T_s denotes the temperature in the solid. On extending the earlier scalings to the energy equation in the solid, there results

$$\frac{k}{\delta}\frac{\partial^2 T_s}{\partial y^2} - \rho c m\frac{\partial T_s}{\partial y} = 0. \tag{19}$$

Integrating this with respect to y and evaluating the result at the interface yields the relation

$$k\frac{\partial T_s}{\partial r} - \rho c m T_s = -\rho L m + k\frac{\partial T}{\partial r} - \rho c m T_f, \tag{20}$$

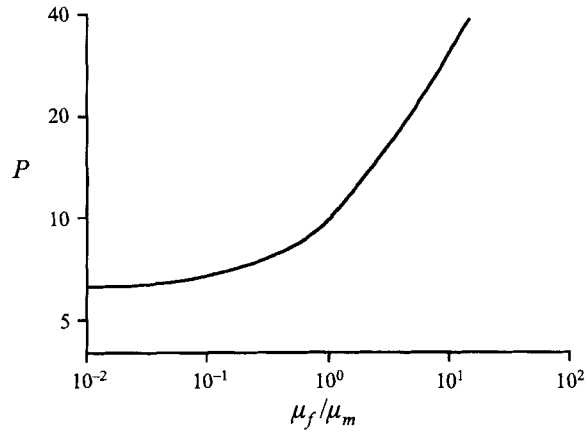

FIGURE 8. The function $P(\mu_{fluid}/\mu_{melt})$, from (Kerr 1994*a*).

where we have used (18). On the other hand, letting $y \to -\infty$ in the integration result yields

$$\frac{k}{\delta}\frac{\partial T_s}{\partial y} - \rho c m T_s = -\rho c m T_0, \tag{21}$$

where we have assumed $\partial T_s/\partial y \to 0$ and $T_s \to T_0$, the initial temperature of the solid. From (20), (21) we finally obtain

$$F_m = k\frac{\partial T}{\partial r} = m\{\rho L + \rho c(T_f - T_0)\} \tag{22}$$

which is the condition (together with (16)) that fixes m.

To summarize, the melting rate m and interfacial temperature T_i are determined by

$$\left.\begin{aligned} 0.7k(T_i - T_f)\left(\frac{g'}{m\nu S}\right)^{1/3} &= \frac{k_w(T_w - T_i)}{2S}\left\{2 + 0.6\left[\frac{8g\beta_w(T_w - T_i)\,S^3}{\nu_w \kappa_w}\right]^{1/4}\right\} \\ \text{and} \qquad 0.7k(T_i - T_f)\left(\frac{g'}{m\nu S}\right)^{1/3} &= m\{\rho L + \rho c(T_f - T_0)\} \end{aligned}\right\} \tag{23}$$

with $S(t) = a - \int_0^t m\,\mathrm{d}t$.

Note that T_i is dependent on the sphere radius, S. The smaller scale of the thermal boundary layer as S reduces results in steeper thermal gradients and higher heat fluxes. Consequently the interfacial temperatures increases.

The above analysis applies to where there is sheet flow of melt. This may be extended to the flow regime where melt detaches as plumes (on the other hemisphere), with the following adaptation. To predict the melt layer thickness we assume that the layer becomes unstable when it reaches a critical thickness. An approximation of this thickness can be obtained using the argument that the time required to grow the melt layer is comparable to the time scale of the finger instability (Lister & Kerr 1989; Kerr & Lister 1992; Kerr 1994*a*), which provides the relationship

$$\bar{\delta} \sim \left(\frac{m\nu P}{g'}\right)^{1/2}, \tag{24}$$

where P is a constant depending on the viscosity ratio of melt and fluid (figure 8). The

c	1340	J kg^{-1} °C^{-1}
k_{magma}	2.89	J m^{-1} s^{-1} °C^{-1}
k_{melt}	2.5	J m^{-1} s^{-1} °C^{-1}
L	2.93×10^5	J kg^{-1}
κ_{magma}	8×10^{-7}	m^2 s^{-1}
β_{magma}	5×10^{-5}	°C^{-1}
μ_{magma}	100	Pa s
μ_{melt}	10^5 (10^4–10^7)	Pa s
ρ_{magma}	2700	kg m^{-3}
ρ_{melt}	2300	kg m^{-3}
T_{magma}	1200 (900–1600)	°C
T_f	850 (750–1000)	°C
T_0	500	°C

TABLE 2. Properties of geological materials. Melt and solid are of granodiorite composition and the magma is basaltic

critical layer thickness is identical for both inclined and horizontal surfaces (Martin & Campbell 1988), so (24) is appropriate for the whole hemisphere. Expressions for m and T_i can now be determined in a similar manner to before. This analysis is not rigorous as the lubrication approximation does not hold where a plume is detaching. Here the melt layer thickness is effectively the length of the plume. Equation (24) provides a reasonable average thickness of melt over the hemisphere. This average will be far less than the sphere radius and so the lubrication approximation is justified when considering the hemisphere as a whole. Consequently the predictions may be moderately accurate.

5. Comparison of theory to experiments

The comparison of theoretical melting rates to the experimental measurements is shown in figure 7. There is excellent agreement between the two. Dissolution of melt occurs in the experiments but is not considered by the theory, so a slight discrepancy between calculated and measured rates is expected. Dissolution will reduce the thickness of the melt layer and hence quicken the melting rate. However, it will have only a very minor effect as the rate of dissolution is so much slower than the melting rate. The consequence of this is that the experimental rates will be marginally faster than the theory. This discrepancy can be inferred from figure 7, where the theory fits best the experimental measurements taken at $\theta = \frac{1}{2}\pi$ (solid crosses). However, as the melt sheet thickness is averaged the best fit may reasonably be expected with measurements taken at $\theta = \frac{1}{4}\pi$; dissolution of melt may account for the slight difference. On the detaching plume hemisphere the theory produces values that are slight overestimates for the hottest fluid temperature.

Theoretical estimates of the average melt sheet thickness, e.g. $\bar{\delta} \sim 0.32$ mm when $T_w = 25$ °C and $\bar{\delta} \sim 0.53$ mm when $T_w = 60$ °C, agree well with the experimental observation of the sheet thickness being up to a maximum of roughly 0.5 mm. Estimates of the critical melt layer thickness on the detaching plume hemisphere are between 0.08 and 0.2 mm.

Comparison of theory to measurements for the experiment where the fluid was $NaNO_3$ solution is shown in figure 6. The relevant comparison is between the gradients of the theoretical lines and the data points; the estimated radii are always slightly less than the measured values as the theory does not consider the brief initial period of

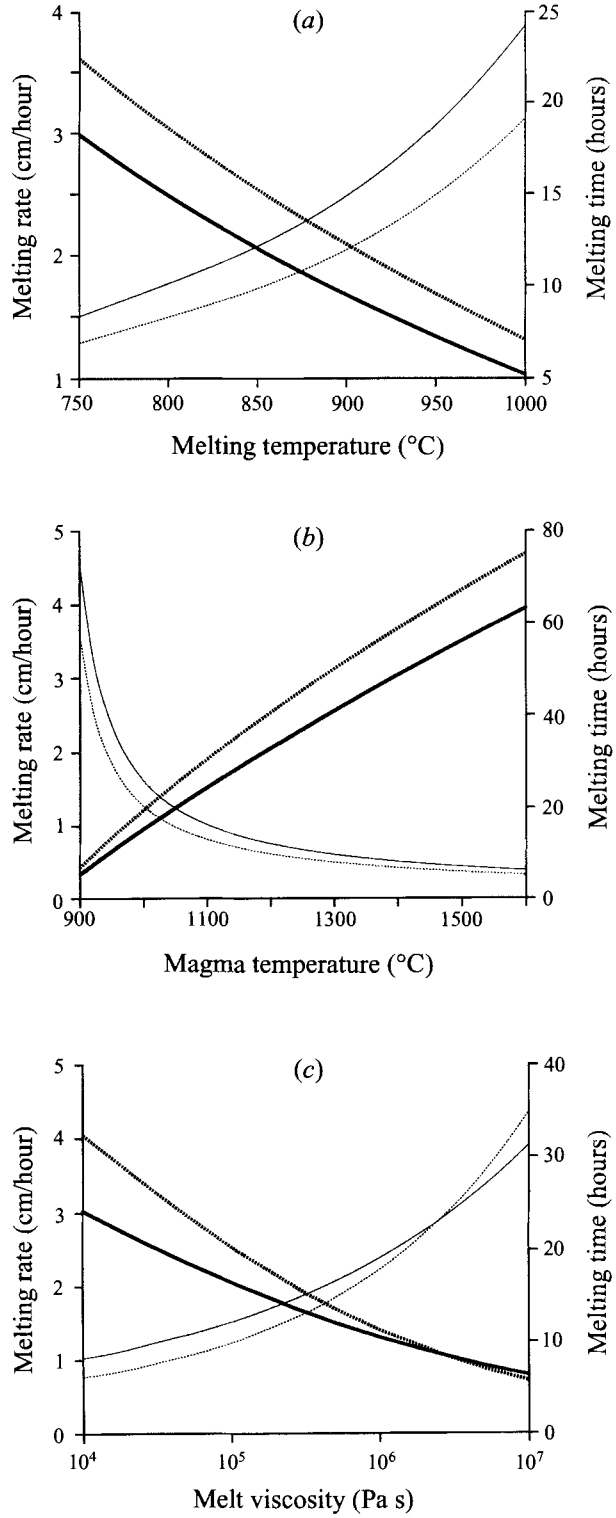

FIGURE 9. Calculated melting rates for xenoliths of 25 cm radius, and the melting time (the time required to completely melt the xenolith), as a function of (*a*) melting temperature (magma temperature fixed at 1200 °C and melt viscosity at 10^5 Pa s), (*b*) magma temperature (melting

relatively slow melting before the rate attains a constant value. Again, there is good agreement of theory and experimental results; opposing flow directions of the melt and thermal boundary layers does not induce inconsistency.

6. Geological applications

The principles developed in this paper can be applied to the interaction between high-temperature (1200 °C) basaltic magma derived from the mantle and the rocks of the continental crust, which typically melt at much lower temperatures (800–1100 °C). Magma chambers develop in the crust where the density of the magma is comparable to the density of the surrounding rocks (Ryan 1987). The margins of these chambers may fracture, and fragments of crustal rock (xenoliths) are incorporated into the magma. Xenoliths are typically observed to be in the size range of 1–0.1 m and these dimensions are probably influenced by the spacing of fractures in the wall rock that pre-existed or formed due to thermal stresses (Furlong & Myers 1985). Once incorporated the xenoliths may melt and thus contaminate the basalt with components of crustal origin. The theoretical model of sphere melting can be applied to this process to calculate how rapidly it can take place. We assume that the crustal fragments can be approximated as spheres and that they are close to neutral buoyancy since the average density of crustal rocks and magma should be similar. Table 2 lists the properties of the relevant geological materials. Note that in the geological application there is a large viscosity contrast between the melt and the magma. Thus the normal criterion for assuming a stress-free interface between the two fluids is well satisfied. Melting rates (and interfacial temperatures) are calculated for the sheet flow hemisphere using (23); for the detaching plume hemisphere, the calculations are performed with equivalent expressions formulated using (24) as an estimate of the melt layer thickness.

For a 25 cm radius xenolith the predicted melting rate on the sheet flow hemisphere is 2.1 cm/hour, so complete melting will have occurred within 12 hours; on the detaching plume hemisphere the predicted melting rate is 2.5 cm/hour, requiring 10 hours for complete assimilation. Estimated steady-state melt layer thicknesses are ~ 4.6 cm on the sheet flow hemisphere and ~ 3.3 cm on the detaching plume hemisphere, thus satisfying the assumption that $\delta/a \ll 1$. Variation of physical parameters within geologically plausible limits does not change the conclusion that xenoliths are rapidly assimilated. The three physical parameters that show significant variations are magmatic temperature, xenolith melting temperature and melt viscosity. Figure 9 shows the estimated melting rates for xenoliths of 25 cm radius for the possible ranges of these properties; also shown is the time required to completely melt the xenolith.

In comparison to the melting rates estimated for xenoliths, Huppert & Sparks (1988*a*–*c*) estimate that melting rates at the roof of a magma chamber are typically a few metres per year. Our calculations imply that the rates of melting of xenoliths can be one to two orders of magnitude higher.

Qualitatively our results are consistent with geological observations. Xenoliths with melting temperatures lower than the host magma are only preserved at the rapidly chilled margins of intrusions and in volcanic rocks where the magma and incorporated

---

temperature fixed at 850 °C and melt viscosity at 10^5 Pa s), and (*c*) melt viscosity (melting temperature fixed at 850 °C and magma temperature at 1200 °C). Melting rates are shown by the thicker curves. Solid curves are for the sheet flow hemisphere and dotted curves for the detaching plume hemisphere. The influence on magma and melt viscosity of varying magma and melting temperatures has been neglected.

xenoliths are erupted (and so frozen) very rapidly before melting can be completed. Basalt magmas erupted through continental crust commonly display geochemical features indicating assimilation of continental crust (e.g. Hildreth & Moorbath 1988), but do not contain intact xenoliths. Plutonic rocks, which represent slowly cooled magma bodies, only contain refractory xenoliths with melting temperatures greater than the host magma.

7. Conclusions

The melting of a solid sphere into hot fluid has been observed in experiments and described by theoretical analysis. The melting rate is controlled by the thermal properties of the solid, the thermal convection of fluid around the body and the compositional convection of the melt produced. Compositional convection of melt around a body can occur in two flow regimes, depending upon the position on the body's surface. Over one half melt flows as a sheet and on the other half it detaches as finger plumes and sinks away mixing into the fluid. The character of the flow controls the thickness of the melt layer, which in turn influences the thermal gradient across it. This, together with the thermal convection of cooled fluid, determines the heat flux to the solid's surface and so the melting rate. A distinctive morphology develops due to differing positional melting rates. Where flow occurs as a sheet of roughly uniform thickness a sphere's surface remains smooth and hemispherical; where melt plumes detach a rough surface is produced by the variations in melt layer thickness, and there is a faster overall rate of melting. The plumes of melt fingers that sink or rise away from the body will become turbulent and mix efficiently with the fluid, unless it first pools against the floor/roof of the chamber that contains the fluid.

The theoretical analysis of both melt flow regimes has provided estimates of the thicknesses of the melt layers. This, together with a consideration of the thermal free convective heat flux from the fluid, allows predictions of the melting rates. These are in good agreement with experimental measurements.

The model is then applied to a geological system: the melting and assimilation of solid blocks of rock incorporated into magmas. Rapid melting rates are predicted, typically in the order of a half metre per day. In addition to this there is efficient mixing of melt into the magma, allowing chemical contamination. This is in contrast to the case of roof melting where melt pools at the top of the chamber and remains compositionally separate. The fast melting rates and relative ease of mixing indicate that this process may be an important factor in magmatic evolution and so in determining the composition and nature of the continental crust and continental magmas.

P.M. is grateful to Ross Kerr for numerous enlightening discussions while visiting the Research School of Earth Sciences, Australian National University, during which the thermal conductivity of PEG 600 melt was measured. We thank one of the referees for some very constructive comments, and Herbert Huppert for reviewing on an earlier draft. R.S.J.S. acknowledges support of the Leverhulme Trust. P.M. was funded by a NERC studentship.

REFERENCES

CAMPBELL, I. H. & TURNER, J. S. 1987 A laboratory investigation of assimilation at the top of a basaltic magma chamber. *J. Geol.* **95**, 155–172.

FANG, D. & HELLAWELL, A. 1988 The surface morphology of crystals melting under solutions of different densities. *J. Cryst. Growth* **92**, 364–370.

FURLONG, K. P. & MYERS, J. D. 1985 Thermal-mechanical modelling of the role of thermal stresses and stoping in magma contamination. *J. Volc. Geotherm. Res.* **24**, 179–191.

HILDRETH, W. & MOORBATH, S. 1988 Crustal contributions to arc magmatism in the Andes of Central Chile. *Contrib. Min. Petrol.* **98**, 455–489.

HUPPERT, H. E. & SPARKS, R. S. J. 1988*a* Melting the roof of a chamber containing a hot turbulently convecting fluid. *J. Fluid Mech.* **188**, 107–131.

HUPPERT, H. E. & SPARKS, R. S. J. 1988*b* The generation of granitic magmas by intrusion of basalt into continental crust. *J. Petrol.* **29**, 599–624.

HUPPERT, H. E. & SPARKS, R. S. J. 1988*c* The fluid dynamics of crystal melting by injection of basaltic sills. *Phil. Trans. R. Soc. Edinburgh: Earth Sci.* **79**, 237–243.

JAFARPUR, K. & YOVANOVICH, M. M. 1992 Laminar free convective heat transfer from isothermal spheres: a new analytical method. *Intl. J. Heat Mass Transfer.* **35**, 2195–2201.

KERR, R. C. 1994*a* Melting driven by vigorous compositional convection. *J. Fluid Mech.* **280**, 255–285.

KERR, R. C. 1994*b* Dissolving driven by vigorous compositional convection. *J. Fluid Mech.* **280**, 287–302.

KERR, R. C. & LISTER, J. R. 1992 Further results for convection driven by the differential sedimentation of particles. *J. Fluid Mech.* **243**, 227–245.

KRANSE, A. A. & SCHENK, J. 1965 Thermal free convection from a solid sphere. *App. Sci. Res.* A **15**, 397–403.

LISTER, J. R. & KERR, R. C. 1987 The effect of geometry on the gravitational instability of a buoyant region of viscous fluid. *J. Fluid Mech.* **202**, 577–594.

MARTIN, D. & CAMPBELL, I. H. 1988 Laboratory modelling of convection in magma chambers: crystallisation against sloping floors. *J. Geophys. Res.* **93**, 7974–7988.

RYAN, M. P. 1987 Neutral buoyancy and the mechanical evolution of magmatic systems. In *Magmatic Processes: Physiochemical Principles* (ed. B. O. Mysen). Geochem. Soc. Spec. Publ., vol. 1, pp. 259–287.

SCHENK, J. & SCHENKELS, F. A. M. 1968 Thermal free convection from an ice sphere in water. *Appl. Sci. Res.* **19**, 465–476.